actuators

Article

Geometry-Adaptive Kinematics and Experimental Validation of a Linear-Actuator-Driven Parallel Lumbar Exoskeleton

Han Xiao [1], Fei Chen [1], Guanbin Gao [2,*], Pengzhen Chen [2] and Qi Li [2]

[1] Faculty of Chemical Engineering, Kunming University of Science and Technology, Kunming 650500, China; xiao_han@stu.kust.edu.cn (H.X.); solarcf@163.com (F.C.)
[2] Yunnan Key Laboratory of Intelligent Control and Application, Faculty of Mechanical and Electrical Engineering, Kunming University of Science and Technology, Kunming 650500, China; pzchen@stu.kust.edu.cn (P.C.); liqi_neo@stu.kust.edu.cn (Q.L.)
* Correspondence: gbgao@kust.edu.cn

Abstract

Wearable lumbar rehabilitation exoskeletons require body-size adaptability and deterministic kinematic modeling. Adjustable wearing structures may alter actuator anchor-point positions, creating inconsistencies in fixed-geometry inverse kinematic models. This study proposes a linear-actuator-driven parallel lumbar exoskeleton using a split semi-ring variable-width platform. Transverse opening increments, h_1 and h_2, are introduced into the anchor-point coordinates to reconstruct the worn geometry. A geometry-adaptive kinematic model is developed to map task-space motions to actuator-space commands. Multibody simulations indicate that compared with a fixed-geometry model, the proposed approach decreases the position RMSE from 1.30 mm to 0.32 mm and the orientation RMSE from 0.62° to 0.05°. Human-worn experiments across three healthy adult male participants yielded a global actuator displacement RMSE of 0.08–0.09 mm, a task-space position RMSE of 4.73–7.64 mm, and an orientation RMSE of 0.71°–1.09°. These task-space errors characterize the exoskeleton-platform motion measured by optical marker clusters rather than directly measured anatomical lumbar-spine kinematics. Rigid testbench validation isolated the kinematic mechanism from human-interface compliance, reducing the testbench position RMSE from 3.07 mm to 1.86 mm and the orientation RMSE from 0.78° to 0.34° compared to the fixed-geometry assumption. These results provide a proof-of-concept validation for the feasibility of the architecture and model for lumbar exoskeletons with transverse width adjustability.

Keywords: lumbar rehabilitation; exoskeleton; parallel mechanism; linear actuator; geometry-adaptive kinematics; transverse adaptation; trajectory tracking

Check for updates

Academic Editor: Zhuming Bi

Received: 28 July 2026
Revised: 1 September 2026
Accepted: 9 September 2026
Published: 12 September 2026

1. Introduction

Low back pain is one of the major causes of long-term activity limitation and rehabilitation demand worldwide. Recent global burden analyses indicate that, although age-standardized rates vary across regions and populations, the absolute number of people affected by low back pain remains substantial [1]. For chronic low back pain, exercise-based rehabilitation and physical therapy interventions are widely recommended, including therapeutic exercise, trunk mobility training, and movement control exercises [2,3]. Specific lumbar exercise directions, such as flexion- and extension-based training, have also been investigated in clinical studies [4]. These studies indicate that lumbar rehabilitation requires repeatable, quantifiable, and direction-specific trunk motion training. However, conventional therapist-assisted rehabilitation is often limited by treatment repeatability, quantitative evaluation, and clinical resource availability. Therefore, robotic lumbar rehabilitation devices provide a promising solution by delivering programmable assistance, standardized motion trajectories, and measurable training processes. For wearable rehabilitation systems, this solution further requires the mechanism to satisfy body-size adaptability, motion safety, and trajectory controllability under human-worn conditions.

Existing wearable back-support devices have been widely investigated for occupational assistance, load reduction, pain relief, and ergonomic support. Passive and quasi-passive devices can reduce metabolic cost, back muscle activity, or lumbar loading during lifting and forward-bending tasks [5–8]. Active wearable lumbar assistance devices have also been developed to provide task-specific support and have been evaluated in terms of lumbar muscle activity, perceived discomfort, pain relief, and in-field ergonomic performance [9–12]. Recent studies and reviews have further extended the evaluation of back-support exoskeletons to complex repetitive tasks, commercial benchmarking, and industrial application scenarios [13–16]. These studies demonstrate the potential of wearable lumbar devices for reducing physical workload and improving ergonomic assistance. Nevertheless, their primary objective is usually to provide external support under specific occupational tasks, rather than to generate prescribed multi-degree-of-freedom trunk motions for rehabilitation. In contrast, lumbar rehabilitation requires the robot to guide repeatable and quantifiable trunk trajectories, including flexion/extension, lateral bending, and compound circumduction motions.

To meet these multi-degree-of-freedom motion requirements, parallel and multi-branch robotic architectures have been explored for spine, lumbar, and trunk rehabilitation. Compared with support-oriented wearable devices, parallel mechanisms can connect the upper trunk and pelvic regions through multiple actuated limbs, thereby providing compact multi-DOF motion generation, high load-carrying capability, and explicit task-to-actuator motion mapping. Stewart–Gough-based robotic spine exoskeletons have been used to control torso posture and characterize three-dimensional trunk stiffness in spine-related rehabilitation scenarios, such as the treatment of spine deformity and scoliosis [17,18]. Other lumbar and trunk rehabilitation robots based on parallel or multi-DOF topologies, such as 4-UPS+PS, 4-SPU/SP, 4-UPS/RRR, and six-degree-of-freedom lumbar exoskeleton systems, have also been developed for lumbar support, lumbar traction, range-of-motion training, workspace analysis, and rehabilitation-oriented trunk motion generation [19–22]. From the perspective of mechanism topology, active wearable lumbar systems can be categorized into belt-based architectures and rigid-platform parallel architectures. Belt-based systems (such as the commercial Japet.W [10], which utilizes four linear actuators coupled via textile belts for lumbar distraction and pain relief) offer high wearing compliance. However, compliant textile interfaces make deterministic multi-DOF anchor-point reconstruction challenging under tightening tension and trunk motion, making such configurations primarily suited for axial unloading rather than deterministic multi-DOF trajectory guidance. In contrast, rigid-platform parallel architectures preserve deterministic anchor coordinates for exact kinematic modeling, but fixed-size frames lack adaptability to inter-subject pelvic and waist width variations. Therefore, existing lumbar devices face a fundamental trade-off between body-size adaptability and deterministic multi-DOF trajectory controllability, which cannot be resolved solely through standard algorithmic recalibration without structural constraints.

This challenge can be summarized as the conflict between body-size adaptability and deterministic actuator-space trajectory generation. More specifically, it can be understood from structural, modeling, and command-generation aspects. At the structural level, flexible or compliant wearing interfaces can adapt to different body shapes and improve wearing comfort, but they cannot always guarantee stable actuator anchor-point coordinates after wearing because of human contact, soft-tissue deformation, and interface sliding. In contrast, fixed-size rigid closed-loop platforms can provide stable geometric references and are convenient for kinematic modeling, but their adaptability to different trunk and pelvic widths is limited. At the modeling level, if the geometric changes introduced by the worn configuration are not considered, the actuator anchor-point coordinates used in the inverse kinematic model may be inconsistent with the actual worn geometry. At the command-generation level, this inconsistency may cause model-induced limb-length errors when prescribed task-space lumbar trajectories are mapped to actuator-space displacement commands, thereby affecting trajectory tracking and motion reproduction in the human-worn configuration. Therefore, the key scientific problem addressed in this study is how to preserve deterministic and measurable actuator anchor-point geometry for actuator-space trajectory generation while allowing a wearable parallel lumbar platform to adapt to user-specific body widths.

To address this problem, this paper proposes a variable-geometry linear-actuator-driven parallel lumbar exoskeleton with split semi-ring platforms and develops a transverse-gap-based kinematic modeling method. The upper and lower platforms are divided into left and right semi-ring modules connected by transverse guide pairs. This structure allows the platform width to adapt to the user's body while preserving locally rigid anchor-point references for the six actuated limbs. The transverse gaps of the upper and lower platforms are measured as h_1 and h_2, respectively, and these measurable geometric variables are introduced into the anchor-point reconstruction model. Based on the reconstructed worn geometry, task-space lumbar rehabilitation trajectories are mapped into actuator-space displacement commands for simulation and human-worn prototype validation.

The main contributions of this work are summarized as follows:

1. A variable-geometry parallel exoskeleton architecture is proposed to address the conflict between body-size adaptability and deterministic kinematic modeling in wearable lumbar rehabilitation systems. The split semi-ring platforms allow transverse adaptation to different users while preserving locally rigid anchor-point references for the six actuated limbs.
2. A transverse-gap-based kinematic modeling method is developed for the proposed wearable parallel mechanism. By introducing the measurable gap variables of the upper and lower platforms, the actuator anchor-point coordinates are explicitly reconstructed, enabling accurate inverse kinematics under user-dependent geometric conditions.
3. An actuator-space trajectory generation and validation framework is established for representative lumbar rehabilitation motions, including flexion/extension, lateral bending, and figure-eight circumduction. The proposed variable-geometry model is evaluated through multibody simulation and human-worn prototype experiments in terms of limb-displacement continuity, actuator-displacement feasibility, and task-space tracking consistency.

The rest of this paper is organized as follows. Section 2 presents the variable-geometry linear-actuator-driven parallel lumbar exoskeleton architecture. Section 3 develops the transverse-gap-based kinematic model and anchor-point reconstruction method. Section 4 describes the task-to-actuator trajectory generation framework. Section 5 reports the multibody simulation studies. Section 6 presents the human-worn prototype experiments. Section 7 discusses the results and limitations. Section 8 concludes this paper.

https://doi.org/10.3390/act15090485

2. Linear-Actuator-Driven Parallel Lumbar Exoskeleton Architecture

This section presents the exoskeleton architecture from the perspective of geometry-adaptive modeling and actuator-space controllability. Rather than describing the hardware as an isolated mechanical assembly, the architecture is analyzed according to its ability to support measurable transverse adaptation, deterministic anchor-point definition, and actuator-space command generation.

2.1. Design Requirements

The proposed exoskeleton is intended to provide repeatable multi-DOF lumbar rehabilitation motions while remaining wearable for users with different body sizes. To achieve this objective, three design requirements are considered.

First, the structure should provide body-size adaptability. The width of the waist–pelvis region varies among users, and a fixed closed-loop rigid frame may therefore lead to poor fit or unstable contact. Accordingly, the upper and lower platforms should allow transverse adaptation during wearing.

Second, the structure should maintain deterministic anchor-point geometry. For a parallel mechanism, the attachment-point coordinates directly determine the inverse kinematic solution. If the anchor points are mainly supported by flexible straps or deformable soft interfaces, their positions may drift under load, thereby reducing modeling accuracy. Therefore, the actuator attachment points should be located on locally rigid modules.

Third, the system should support actuator-space controllability. The desired lumbar motion must be converted into displacement, velocity, and axial force commands for the six linear actuators. Thus, the architecture should provide clearly defined actuator-space variables and measurable geometric parameters for real-time command generation.

2.2. Overall Parallel Architecture

Based on the above requirements, the proposed exoskeleton consists of an upper platform, a lower platform, six integrated linear actuators, and a binding interface. The lower platform is worn around the pelvis region, whereas the upper platform is worn around the upper trunk. The six linear actuators connect the upper and lower platforms through 6-UPS (universal-prismatic-spherical) joint configurations, enabling the upper platform to move relative to the lower platform in six degrees of freedom. In the kinematic model, the lower platform is treated as the base, and the upper platform is treated as the moving platform.

During rehabilitation, the target lumbar motion is described as a desired task-space pose of the upper platform relative to the lower platform. This spatial motion comprises three rotational components and three translational components of the human trunk, which are directly realized by the 6-UPS parallel architecture. The geometry-adaptive inverse kinematics then maps this desired pose into six actuator-space references. In this way, the linear-actuator-driven parallel architecture provides the mechanical basis for converting task-space rehabilitation trajectories into actuator commands.

2.3. Split Semi-Ring Platform and Transverse Adaptation

To improve body-size adaptability while preserving anchor-point determinacy, a split semi-ring adaptive platform is designed, as shown in Figure 1. Both the upper and lower platforms are composed of left and right symmetric semi-ring modules. These two semi-rings are connected by transverse linear guide pairs. The semi-ring bodies provide locally rigid references for the branch attachment points, whereas the guide pairs release the transverse width constraint and allow the platform to adapt to the user's body size during wearing.

https://doi.org/10.3390/act15090485

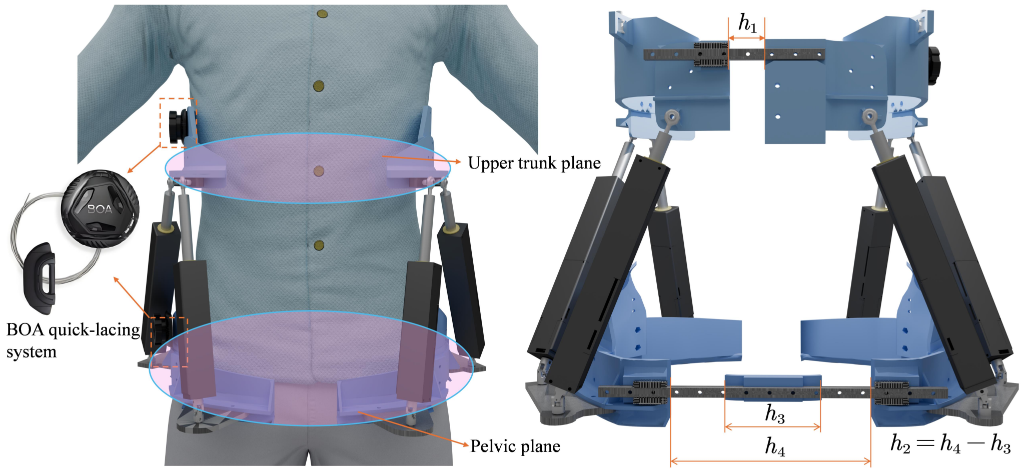

Figure 1. Split semi-ring platform and transverse adaptation mechanism.

The platform locking force is provided by a BOA lacing system. During wearing, cable tension pulls the left and right semi-ring modules toward the human body until stable contact is formed between the support surfaces and the body. After locking, the lateral relative motion of the semi-rings is constrained by cable tension and human contact, allowing the structure to behave as a six-DOF parallel mechanism with stable hinge geometry. Thus, the guide sliding mechanism accommodates body-width variation, while the hinge points remain mounted on rigid modules rather than directly on deformable soft straps.

Let the effective transverse gap of the upper platform be denoted by h_1 and that of the lower platform by h_2. Specifically for the lower platform, as illustrated in Figure 1, this effective gap is determined by $h_2 = h_4 - h_3$. Here, h_4 represents the total physical distance between the left and right semi-ring modules, and h_3 denotes the constant width of the central fixed spacer. These gap parameters characterize the geometric changes generated during the wearing and locking process. They are later used as inputs for reconstructing the upper and lower anchor-point coordinates.

2.4. Linear Actuation Unit and Actuator-Space Variables

Six integrated linear actuators are used as active branches. To meet the requirements of compactness, stroke range, and response speed in wearable rehabilitation systems, a compact motor–screw actuator is designed, as shown in Figure 2. The actuator mainly consists of a miniature brushless DC motor, a ball screw, a magnetic encoder, a film displacement sensor, and an embedded motor driver board. The motor and ball screw are arranged coaxially, which reduces intermediate transmission elements and improves structural integration.

The magnetic encoder measures the motor rotor position, while the film displacement sensor measures the absolute linear displacement of the push rod. The driver board integrates a three-phase inverter, current sensing, and a microcontroller, thereby enabling local current-loop control and state acquisition. Through an FDCAN bus, the host computer sends target position, target velocity, stiffness, damping, and feedforward force commands to each actuator and receives actuator position, velocity, and motor state feedback.

https://doi.org/10.3390/act15090485

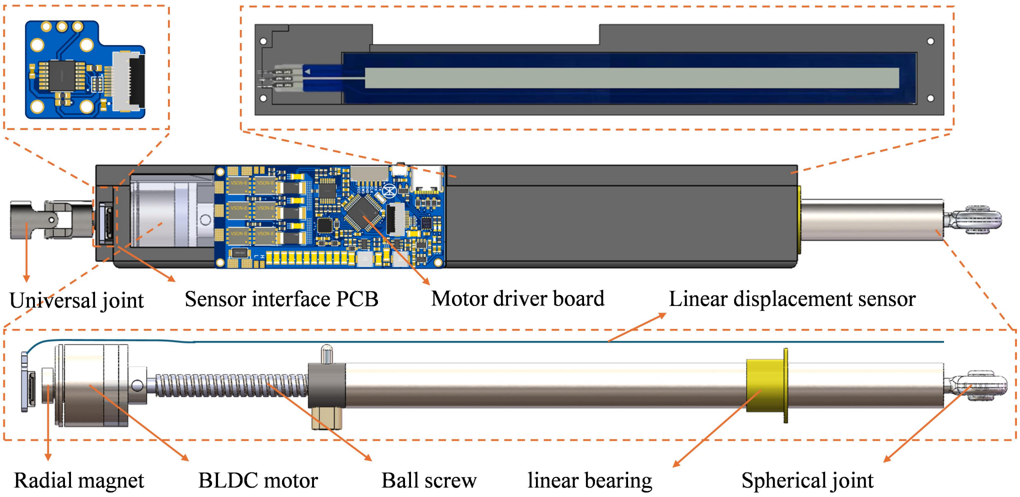

Figure 2. Integrated linear actuation unit.

For the ith actuator, let θ_i be the motor output angle, and p_s be the screw lead. In the kinematic model, l_i represents the theoretical branch length (i.e., the Euclidean distance between the upper and lower anchor points), and l_{i0} is this theoretical length at the neutral pose. In the physical implementation, the film displacement sensor provides an absolute position reading s_i relative to its hardware zero-position, with s_{i0} being the initial sensor reading at the neutral pose.

To bridge the kinematic model and the hardware measurement, the actuator-space variables are defined as

$$s_i = s_{i0} + \frac{p_s}{2\pi}\theta_i, \qquad q_i = s_i - s_{i0} = l_i - l_{i0}, \qquad \dot{q}_i = \frac{p_s}{2\pi}\dot{\theta}_i, \tag{1}$$

where q_i is the relative actuator displacement. By defining q_i as the displacement relative to the neutral pose, the constant mechanical offset between the theoretical branch length and the sensor's physical installation zero is inherently canceled out ($l_i - l_{i0} = s_i - s_{i0}$).

Consequently, q_i serves as the command variable for kinematic mapping and tracking control. Note that to accurately reflect the true mechanical state of the device, the absolute sensor reading s_i is utilized to depict the stroke limits and experimental actuator trajectories in the subsequent sections.

Let τ_i be the motor output torque and η be the transmission efficiency. Neglecting friction and inertia, the axial output force F_i is approximated by

$$F_i = \frac{2\pi\eta}{p_s}\tau_i. \tag{2}$$

The motor uses field-oriented control, and the q-axis current is treated as the torque-producing current:

$$\tau_i = K_t I_{q,i}, \qquad F_i = \frac{2\pi\eta K_t}{p_s} I_{q,i}, \tag{3}$$

where K_t is the motor torque constant and $I_{q,i}$ is the q-axis current. Equations (1)–(3) define the actuator-space displacement, velocity, and force variables used in the subsequent trajectory tracking implementation.

According to the selected hardware parameters, the rated torque of the 1806 brushless motor is approximately 0.03 N · m, the rated speed is 800 rpm, the screw lead is 0.001 m, and the comprehensive transmission efficiency is approximately 0.9. Based on these parameters, the rated linear velocity and continuous output force of a single actuator are calculated as

$$\dot{q}_r = \frac{n_r p_s}{60} \approx 13.33 \text{ mm/s}, \tag{4}$$

$$F_r = \frac{2\pi\eta\tau_r}{p_s} \approx 169.65 \text{ N}. \tag{5}$$

These calculations indicate that the compact actuator can provide a theoretical continuous output capacity of approximately 170 N for each branch (with motor torque constant $K_t = 0.06 \text{ N} \cdot \text{m/A}$), which serves solely as an idealized theoretical benchmark of actuator power margin neglecting transmission friction and dynamic loads, rather than an experimentally validated force capability.

3. Geometry-Adaptive Kinematic Modeling

This section derives the geometry-adaptive kinematic model of the proposed linear-actuator-driven parallel lumbar exoskeleton. Specifically, the term "geometry-adaptive" refers to a configuration-dependent kinematic parameterization based on the measured transverse gaps after wearing and locking, rather than online geometric adaptation during motion. Since the upper and lower platforms can be opened laterally during wearing, the transverse gap parameters h_1 and h_2 are explicitly introduced into the anchor-point coordinates. Here, h_1 and h_2 denote the additional transverse gaps of the upper and lower platforms relative to the fully closed configuration, respectively. Therefore, $h_1 = 0$ and $h_2 = 0$ correspond to the closed upper and lower platforms.

3.1. Coordinate Systems and Nominal Anchor Points

A base coordinate frame $\{B\}$ and a moving platform coordinate frame $\{P\}$ are defined on the lower and upper platforms, respectively, as shown in Figure 3. The origin O_B of $\{B\}$ is located at the nominal geometric center of the lower platform. The X_B axis points toward the front of the human body, the Y_B axis is along the transverse guide direction and points to the left side of the human body, and the Z_B axis is normal to the lower platform plane. Similarly, the origin O_P of $\{P\}$ is located at the nominal geometric center of the upper platform. In the neutral pose, the axes of $\{P\}$ are parallel to those of $\{B\}$.

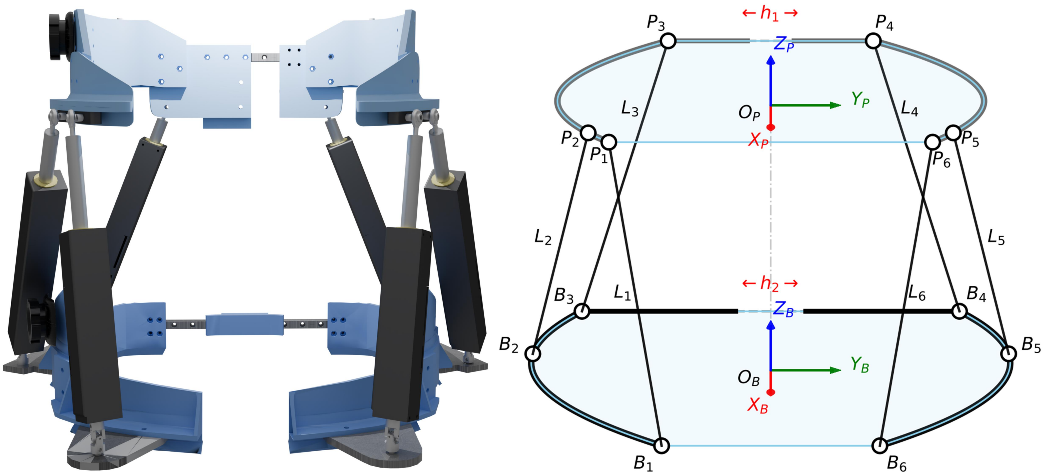

Figure 3. Coordinate systems and anchor-point definition.

Let B_i and P_i denote the lower and upper anchor points of the ith branch, respectively. Since the nominal anchor-point coordinates are measured when the upper and lower platforms are fully closed, their coordinate vectors under the closed reference configuration are defined as

$$\mathbf{b}_i^0 = \begin{bmatrix} x_{bi}^0 & y_{bi}^0 & z_{bi}^0 \end{bmatrix}^{\mathrm{T}}, \qquad \mathbf{p}_i^0 = \begin{bmatrix} x_{pi}^0 & y_{pi}^0 & z_{pi}^0 \end{bmatrix}^{\mathrm{T}}, \quad i = 1, 2, \ldots, 6. \tag{6}$$

Here, the superscript 0 denotes the closed reference configuration.

3.2. Anchor-Point Reconstruction with Transverse Gaps

During wearing, the left and right semi-ring modules slide symmetrically along the Y direction. Therefore, an additional transverse gap produces a displacement of half of the gap value on each side. The side signs of the upper and lower anchor points are defined as

$$s_{pi} = \operatorname{sgn}\left(y_{pi}^0\right), \qquad s_{bi} = \operatorname{sgn}\left(y_{bi}^0\right), \qquad s_{pi}, s_{bi} \in \{-1, 1\}. \tag{7}$$

Accordingly, when the additional transverse gaps of the upper and lower platforms are h_1 and h_2, the reconstructed anchor-point coordinates are written as

$$\mathbf{p}_i(h_1) = \begin{bmatrix} x_{pi}^0 \\ y_{pi}^0 + s_{pi}\dfrac{h_1}{2} \\ z_{pi}^0 \end{bmatrix}, \qquad \mathbf{b}_i(h_2) = \begin{bmatrix} x_{bi}^0 \\ y_{bi}^0 + s_{bi}\dfrac{h_2}{2} \\ z_{bi}^0 \end{bmatrix}. \tag{8}$$

Equation (8) converts the wearing-induced transverse opening into explicit variations of the anchor-point coordinates.

3.3. Geometry-Adaptive Inverse Kinematics

Let the pose of the moving platform frame $\{P\}$ relative to the base frame $\{B\}$ be described by the translation vector $\mathbf{t}$ and the rotation matrix $\mathbf{R}$:

$$\mathbf{t} = \begin{bmatrix} x & y & z \end{bmatrix}^{\mathrm{T}}, \qquad \mathbf{R} = \mathbf{R}_z(\gamma)\mathbf{R}_y(\beta)\mathbf{R}_x(\alpha). \tag{9}$$

Here, α, β, and γ denote the roll, pitch, and yaw angles about the X, Y, and Z axes, respectively. The rotation matrix is expressed using the ZYX sequence.

For the ith branch, the upper anchor point expressed in the base frame is

$${}^{B}\mathbf{p}_i = \mathbf{t} + \mathbf{R}\mathbf{p}_i(h_1). \tag{10}$$

Thus, the branch vector of the ith actuator is

$$\mathbf{L}_i = {}^{B}\mathbf{p}_i - \mathbf{b}_i(h_2) = \mathbf{t} + \mathbf{R}\mathbf{p}_i(h_1) - \mathbf{b}_i(h_2). \tag{11}$$

The corresponding branch length is

$$l_i = \|\mathbf{L}_i\| = \|\mathbf{t} + \mathbf{R}\mathbf{p}_i(h_1) - \mathbf{b}_i(h_2)\|. \tag{12}$$

For actuator-space command generation, the actuator displacement is defined relative to the neutral pose under the same worn configuration. Let the neutral pose be denoted by $\mathbf{t}_0$ and $\mathbf{R}_0$. The reference branch length is then

$$l_{i0} = \|\mathbf{t}_0 + \mathbf{R}_0\mathbf{p}_i(h_1) - \mathbf{b}_i(h_2)\|. \tag{13}$$

https://doi.org/10.3390/act15090485

Therefore, the actuator displacement command of the ith branch is

$$q_i = l_i - l_{i0}. \tag{14}$$

Equations (8)–(14) constitute the geometry-adaptive inverse kinematic model. Compared with a fixed-geometry model, this model updates the branch lengths according to the transverse openings of the upper and lower platforms.

3.4. Comparison with a Nominal Fixed-Geometry Model

For comparison, a nominal fixed-geometry baseline is defined using constant default transverse gaps of $\bar{h}_1 = 20$ mm and $\bar{h}_2 = 30$ mm. These values correspond to the nominal mid-range opening state of the transverse slide guides during initial CAD dimensioning. In a conventional unadapted control scheme, inverse kinematics typically assumes such fixed nominal dimensions. Contrasting the proposed model against this baseline illustrates the magnitude of model-induced kinematic distortions when user-specific worn geometry is neglected. The corresponding fixed anchor-point coordinates are defined as $\mathbf{p}_i^{\text{fix}} = \mathbf{p}_i(\bar{h}_1)$ and $\mathbf{b}_i^{\text{fix}} = \mathbf{b}_i(\bar{h}_2)$. Consequently, the fixed-geometry branch vector and branch length are given by

$$\mathbf{L}_i^{\text{fix}} = \mathbf{t} + \mathbf{R}\mathbf{p}_i^{\text{fix}} - \mathbf{b}_i^{\text{fix}}, \qquad l_i^{\text{fix}} = \left\| \mathbf{L}_i^{\text{fix}} \right\|. \tag{15}$$

The corresponding reference branch length at the neutral pose is calculated as

$$l_{i0}^{\text{fix}} = \left\| \mathbf{t}_0 + \mathbf{R}_0\mathbf{p}_i^{\text{fix}} - \mathbf{b}_i^{\text{fix}} \right\|. \tag{16}$$

Thus, the fixed-geometry actuator displacement command is

$$q_i^{\text{fix}} = l_i^{\text{fix}} - l_{i0}^{\text{fix}}. \tag{17}$$

The geometric mismatch between the geometry-adaptive command q_i and the fixed-geometry command q_i^{fix} directly governs the task-space motion fidelity. Although forward kinematics is not required for error evaluation in this study due to direct optical motion-capture measurements, it can be formulated consistently via the kinematic loop constraints $\Phi_i(\mathbf{t}, \mathbf{R}) = \|\mathbf{t} + \mathbf{R}\mathbf{p}_i(h_1) - \mathbf{b}_i(h_2)\|^2 - l_i^2 = 0$ $(i = 1, \ldots, 6)$.

To analytically evaluate the kinematic sensitivity of the platform pose to transverse gap variations, the complete differential mapping is established. For a small platform translation perturbation $\delta\mathbf{t}$, a small rotation vector perturbation $\delta\boldsymbol{\phi}$, and unmodeled gap discrepancies $\delta\mathbf{h} = [\delta h_1, \delta h_2]^{\mathrm{T}}$, differentiating the branch length $l_i = \|\mathbf{L}_i\|$ yields the first-order variation:

$$\delta l_i = \mathbf{u}_i^{\mathrm{T}}\delta\mathbf{t} + (\mathbf{R}\mathbf{p}_i \times \mathbf{u}_i)^{\mathrm{T}}\delta\boldsymbol{\phi} + \frac{1}{2}s_{pi}\mathbf{u}_i^{\mathrm{T}}\mathbf{R}\mathbf{e}_y\delta h_1 - \frac{1}{2}s_{bi}u_{iy}\delta h_2, \tag{18}$$

where $\mathbf{u}_i = \mathbf{L}_i / l_i$ is the branch unit vector, $\mathbf{e}_y = [0, 1, 0]^{\mathrm{T}}$, and u_{iy} is the transverse projection of $\mathbf{u}_i$. Stacking Equation (18) for all six limbs yields the overall differential system:

$$\delta\mathbf{l} = \mathbf{J}_x\delta\mathbf{x} + \mathbf{J}_h\delta\mathbf{h}, \tag{19}$$

where $\delta\mathbf{x} = [\delta\mathbf{t}^{\mathrm{T}}, \delta\boldsymbol{\phi}^{\mathrm{T}}]^{\mathrm{T}} \in \mathbb{R}^6$, and the i-th rows of the platform Jacobian $\mathbf{J}_x \in \mathbb{R}^{6\times 6}$ and gap sensitivity matrix $\mathbf{J}_h \in \mathbb{R}^{6\times 2}$ are explicitly defined as

$$\mathbf{J}_{x,i} = \begin{bmatrix} \mathbf{u}_i^{\mathrm{T}} & (\mathbf{R}\mathbf{p}_i \times \mathbf{u}_i)^{\mathrm{T}} \end{bmatrix}, \qquad \mathbf{J}_{h,i} = \begin{bmatrix} \frac{1}{2}s_{pi}\mathbf{u}_i^{\mathrm{T}}\mathbf{R}\mathbf{e}_y & -\frac{1}{2}s_{bi}u_{iy} \end{bmatrix}. \tag{20}$$

When the actuators execute branch-length commands generated from an unadapted geometric baseline ($\delta\mathbf{l} = \mathbf{0}$), the model-induced task-space pose deviation caused by gap discrepancies $\delta\mathbf{h}$ is governed by $\delta\mathbf{x} = -\mathbf{J}_x^{-1}\mathbf{J}_h\delta\mathbf{h}$. Because the side signs $s_{pi}, s_{bi} \in \{-1, 1\}$ are anti-symmetric across the sagittal plane (positive on the left, negative on the right), an unmodeled transverse gap discrepancy $(\delta h_1, \delta h_2)$ induces opposite differential displacement variations on contralateral branches ($\delta l_{\text{left}} \approx -\delta l_{\text{right}}$). Acting through the longitudinal moment arms ($x_{pi}^0 \neq 0$), this bilateral push–pull actuation predominantly generates a rotational couple about the vertical Z-axis (yaw) via the inverse Jacobian mapping $-\mathbf{J}_x^{-1}$. In contrast, pitch rotation requires anterior–posterior differential actuation and is decoupled from transverse opening variations since s_{pi} and s_{bi} are independent of the longitudinal coordinates, while roll rotation is constrained by vertical branch geometry. This analytical formulation proves that yaw orientation is the primary component sensitive to transverse gap errors, demonstrating that explicitly updating h_1 and h_2 is mathematically essential to eliminate systematic contralateral kinematic distortion across diverse body sizes.

4. Geometry-Adaptive Task-to-Actuator Trajectory Generation and Tracking Implementation

The desired lumbar rehabilitation motion is first generated in task space and then mapped into actuator displacement commands through the geometry-adaptive inverse kinematics. This section describes a practical actuator-space trajectory tracking framework to validate the proposed mechanism and kinematic model.

4.1. Task-Space Rehabilitation Trajectory Generation

Spinal biomechanical studies demonstrate that the instantaneous center of rotation (ICR) of lumbar motion segments remains confined within a localized spatial envelope during conservative flexion movements [23]. From an engineering and rehabilitation standpoint, gross trunk articulation during standardized exercises can thus be reasonably parameterized relative to an equivalent fixed virtual center of rotation, with residual biological deviations buffered by interface compliance. To generate repeatable and adjustable lumbar rehabilitation trajectories, this study uses parameterized functions to describe the desired task-space motion of the upper platform. Since flexion/extension is commonly used in lumbar exercise interventions for chronic low back pain [4], flexion/extension, lateral bending, and figure-eight circumduction are selected as representative rehabilitation trajectories.

The lumbar motion of the human–exoskeleton system is approximated as a rotation of the upper platform around an equivalent rehabilitation center. The rehabilitation motion is described by flexion/extension, lateral bending, and axial rotation components, denoted by $\theta_f(t)$, $\theta_l(t)$, and $\theta_a(t)$, respectively.

To represent asymmetric motion amplitudes in opposite directions, the following periodic function is defined:

$$\Phi(t; A^+, A^-) = \begin{cases} A^+ \sin(\omega t), & \sin(\omega t) \geq 0, \\ A^- \sin(\omega t), & \sin(\omega t) < 0, \end{cases} \tag{21}$$

where A^+ and A^- are the positive and negative angular amplitudes, respectively, and ω is the angular frequency. In practical control implementation, a low-pass trajectory filter (second-order Butterworth filter, 1.0 Hz cutoff) is applied to this theoretical reference to smooth the velocity transition at the zero-crossing, thereby preventing mechanical jerks and ensuring safe human–exoskeleton interaction. To ensure physiological safety, target angular amplitudes are strictly restricted within 30–50% of normal human anatomical limits (detailed in Section 6).

https://doi.org/10.3390/act15090485

For flexion/extension and lateral bending trajectories, the angular references are given by

$$\begin{aligned} \text{Flexion/extension:} \quad & \theta_f(t) = \Phi(t; A_f, A_e), \quad \theta_l(t) = 0, \quad \theta_a(t) = 0, \\ \text{Lateral bending:} \quad & \theta_l(t) = \Phi(t; A_l, A_r), \quad \theta_f(t) = 0, \quad \theta_a(t) = 0. \end{aligned} \tag{22}$$

For compound rehabilitation trajectories, the angular functions in the three directions can be combined as:

$$\theta_f(t) = g_f(t), \quad \theta_l(t) = g_l(t), \quad \theta_a(t) = g_a(t). \tag{23}$$

To evaluate the system's capability in tracking fully coupled spatial motions, the figure-eight circumduction trajectory is constructed by combining all three directional components. Specifically, the functions are defined with a synchronized frequency relationship as $g_f(t) = A_f \sin(\omega t)$, $g_l(t) = A_l \sin(2\omega t)$, and $g_a(t) = A_a \sin(\omega t)$.

Let the equivalent rehabilitation center and the neutral moving-platform center be

$$\mathbf{C} = \begin{bmatrix} C_x & C_y & H_c \end{bmatrix}^{\mathrm{T}}, \qquad \mathbf{p}_0 = \begin{bmatrix} X_0 & Y_0 & H \end{bmatrix}^{\mathrm{T}}. \tag{24}$$

The desired rotation matrix is constructed as

$$\mathbf{R}_d(t) = \mathbf{R}_z(\theta_a(t))\mathbf{R}_y\Big(\theta_f(t)\Big)\mathbf{R}_x(\theta_l(t)), \tag{25}$$

which is consistent with the ZYX rotation sequence used in the kinematic model. The desired position of the moving-platform center is calculated as

$$\mathbf{p}_d(t) = \mathbf{C} + \mathbf{R}_d(t)(\mathbf{p}_0 - \mathbf{C}). \tag{26}$$

Thus, $\mathbf{p}_d(t)$ and $\mathbf{R}_d(t)$ provide the task-space input for actuator-space command generation. The equivalent rehabilitation center $\mathbf{C}$ is estimated in the mid-sagittal plane at the lumbar region relative to the lower base platform. The prescribed angular trajectory $\mathbf{R}_d(t)$ is independent of this choice, while the derived platform translation satisfies $\delta\mathbf{p}_d(t) = (\mathbf{I} - \mathbf{R}_d(t))\delta\mathbf{C}$. For the prescribed rehabilitation ranges ($\theta \leq 24.0°$), the translational perturbation is geometrically attenuated by $\|\mathbf{I} - \mathbf{R}_d(t)\| \leq 2\sin(\theta/2) \leq 2\sin(12.0°) \approx 0.42$, ensuring that moderate center estimation offsets ($\|\delta\mathbf{C}\| \leq 20$ mm) produce only sub-centimeter relative displacements ($\leq$8.3 mm) that are buffered by strapping interface compliance, while actuator displacement feasibility is verified via prior kinematic simulations.

4.2. Geometry-Adaptive Task-to-Actuator Mapping

For the ith actuator, the desired branch length under the current worn configuration is calculated as

$$l_{d,i}(t) = \|\mathbf{p}_d(t) + \mathbf{R}_d(t)\mathbf{p}_i(h_1) - \mathbf{b}_i(h_2)\|. \tag{27}$$

The neutral branch length under the same transverse gaps is

$$l_{i0} = \|\mathbf{p}_0 + \mathbf{R}_0\mathbf{p}_i(h_1) - \mathbf{b}_i(h_2)\|, \tag{28}$$

where $\mathbf{R}_0$ is the neutral rotation matrix. Therefore, the desired actuator displacement is

$$q_{d,i}(t) = l_{d,i}(t) - l_{i0}. \tag{29}$$

In implementation, rather than deriving a complex Jacobian matrix for analytical velocity mapping, the desired actuator velocity is explicitly generated via numerical differentiation of the smoothed displacement sequence:

$$\dot{q}_{d,i}(k) = \frac{q_{d,i}(k) - q_{d,i}(k-1)}{\Delta t}. \tag{30}$$

This position-level mapping and subsequent numerical differentiation convert task-space rehabilitation trajectories into actuator-space position and velocity references while accounting for the transverse openings h_1 and h_2.

4.3. Actuator-Space Tracking Implementation

Based on the geometry-adaptive task-to-actuator mapping described above, the desired actuator displacement $q_{d,i}$ and desired actuator velocity $\dot{q}_{d,i}$ are obtained for each linear actuator. The proposed exoskeleton is controlled in actuator space rather than by directly controlling the moving-platform pose. This strategy avoids solving a coupled platform-level force distribution problem and allows each integrated linear actuator to perform local displacement tracking.

For the ith actuator, the position and velocity tracking errors at the kth sampling instant are defined as

$$e_i(k) = q_{d,i}(k) - q_i(k), \qquad \dot{e}_i(k) = \dot{q}_{d,i}(k) - \dot{q}_i(k), \tag{31}$$

where $q_i(k)$ and $\dot{q}_i(k)$ are the measured displacement and velocity of the actuator, respectively.

To achieve practical tracking in the presence of unmodeled hardware friction and local mechanical disturbances, a proportional-derivative (PD) feedback control scheme augmented with a feedforward compensation term is utilized on the embedded driver. The final actuator-space force command is obtained as

$$F_i(k) = K_{p,i}e_i(k) + K_{d,i}\dot{e}_i(k) + F_{c,i}(k), \tag{32}$$

where $K_{p,i}$ and $K_{d,i}$ are the linear position stiffness and velocity damping coefficients, respectively. To counteract lumped mechanical friction during physical testing, the feedforward term $F_{c,i}(k)$ is implemented by adopting the Unknown System Dynamics Estimator (USDE) framework [24]. By employing this existing filtering technique locally on the motor driver, the actuator can better follow the geometric commands without requiring an explicit dynamic model of the complete human–exoskeleton coupled system.

In implementation, the host computer sends the desired displacement $q_{d,i}$, desired velocity $\dot{q}_{d,i}$, position stiffness $K_{p,i}$, velocity damping $K_{d,i}$, and the feedforward term $F_{c,i}$ to each integrated actuator through the FDCAN bus. Finally, the desired axial force is converted into the q-axis current command of the brushless motor according to the ball-screw transmission relationship:

$$I_{q,i}(k) = \frac{p_s}{2\pi\eta K_t} F_i(k), \tag{33}$$

where p_s is the screw lead, η is the transmission efficiency, and K_t is the motor torque constant.

4.4. Real-Time Control Implementation

The host computer performs task-space trajectory generation, geometry-adaptive inverse kinematics, actuator-space reference generation, and command transmission. For each actuator, the transmitted command contains the desired displacement $q_{d,i}$, desired velocity $\dot{q}_{d,i}$, stiffness coefficient $K_{p,i}$, damping coefficient $K_{d,i}$, and compensation force $F_{c,i}$. Each integrated actuator performs local position sensing, current-loop control, and motor driving. The measured actuator displacement, velocity, and motor state are then transmitted back to the host computer through the FDCAN bus.

4.5. Performance Evaluation Metrics

To evaluate the tracking performance in both simulation and prototype experiments, identical evaluation metrics are defined for actuator space and task space.

For the ith actuator, the tracking error at the kth sampling instant is $e_{q_i}(k) = q_{d,i}(k) - q_i(k)$. For a trajectory with N samples, the global actuator displacement root-mean-square error (RMSE) and maximum error are defined as

$$\mathrm{RMSE}_q = \sqrt{\frac{1}{6N}\sum_{i=1}^{6}\sum_{k=1}^{N} e_{q_i}^2(k)}, \qquad e_q^{\max} = \max_{i,k}\left|e_{q_i}(k)\right|. \tag{34}$$

In the task space, let $\mathbf{p}_d(k)$ and $\mathbf{R}_d(k)$ denote the desired position and rotation matrix, respectively, while $\mathbf{p}_m(k)$ and $\mathbf{R}_m(k)$ denote the measured (or simulated) position and rotation matrix. To avoid the singularity and coupling issues associated with Euler angles, the task-space orientation error is calculated using the geodesic distance on SO(3). The task-space position error $e_p(k)$ and orientation error $e_R(k)$ are calculated as

$$e_p(k) = \|\mathbf{p}_m(k) - \mathbf{p}_d(k)\|, \qquad e_R(k) = \cos^{-1}\left[\frac{\mathrm{tr}\left(\mathbf{R}_d^{\mathrm{T}}(k)\mathbf{R}_m(k)\right) - 1}{2}\right]. \tag{35}$$

The orientation error is converted to degrees for analysis. The corresponding task-space position and orientation RMSEs are calculated as

$$\mathrm{RMSE}_p = \sqrt{\frac{1}{N}\sum_{k=1}^{N} e_p^2(k)}, \qquad \mathrm{RMSE}_R = \sqrt{\frac{1}{N}\sum_{k=1}^{N} e_R^2(k)}. \tag{36}$$

5. Simulation Studies

Simulation studies are conducted to evaluate displacement feasibility and the effect of geometry-adaptive anchor-point reconstruction under representative lumbar rehabilitation trajectories.

5.1. Simulation Setup

A multibody simulation model of the exoskeleton is built in Simscape Multibody, as shown in Figure 4. The model includes the upper platform, lower platform, six linear actuator branches, and the corresponding hinge constraints. The actuators are driven by position inputs generated from the inverse kinematic model.

https://doi.org/10.3390/act15090485

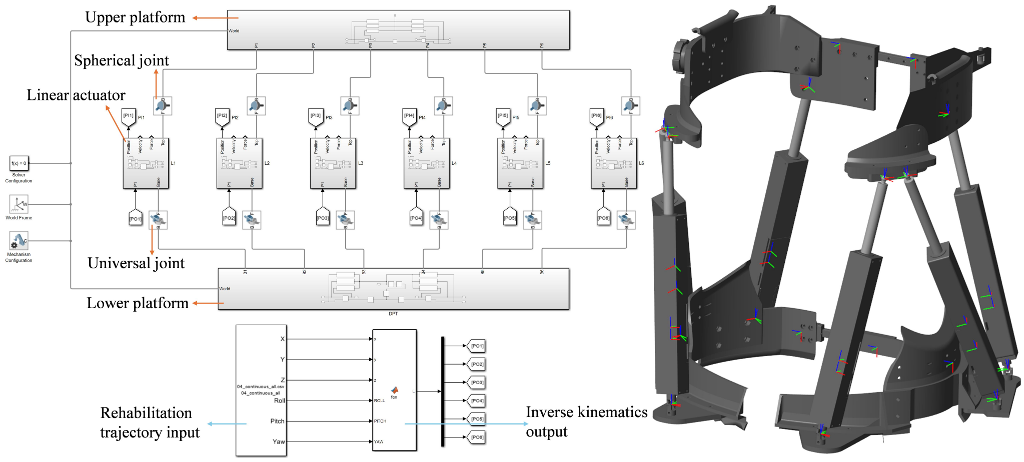

Figure 4. Multibody simulation model of the lumbar rehabilitation exoskeleton.

The three rehabilitation trajectories defined in Section 4, namely flexion/extension, lateral bending, and figure-eight circumduction, are used as simulation inputs. To comprehensively evaluate the influence of geometric mismatch, five simulation cases are designed based on different combinations of the actual worn geometry and the kinematic model assumption. Specifically, the fixed-geometry model constantly assumes transverse gaps of $h_1 = 20$ mm and $h_2 = 30$ mm regardless of the actual wearing state. In contrast, the geometry-adaptive model updates the anchor-point coordinates according to the measured worn configuration. These models are tested under three actual physical gap conditions: a fully closed state of 0 mm for both platforms, an intermediate state of 20 mm and 30 mm, and a wide state of 54 mm and 73 mm. This wide state directly matches the physical testbench configuration utilized in the subsequent hardware experiments.

5.2. Actuator Displacement Feasibility

The target and simulated actuator displacements are shown in Figure 5. Since the actuators are driven by ideal position inputs in the multibody simulation, this figure is mainly used to verify displacement feasibility rather than actuator-level tracking performance. The upper and lower stroke limits are also plotted for comparison.

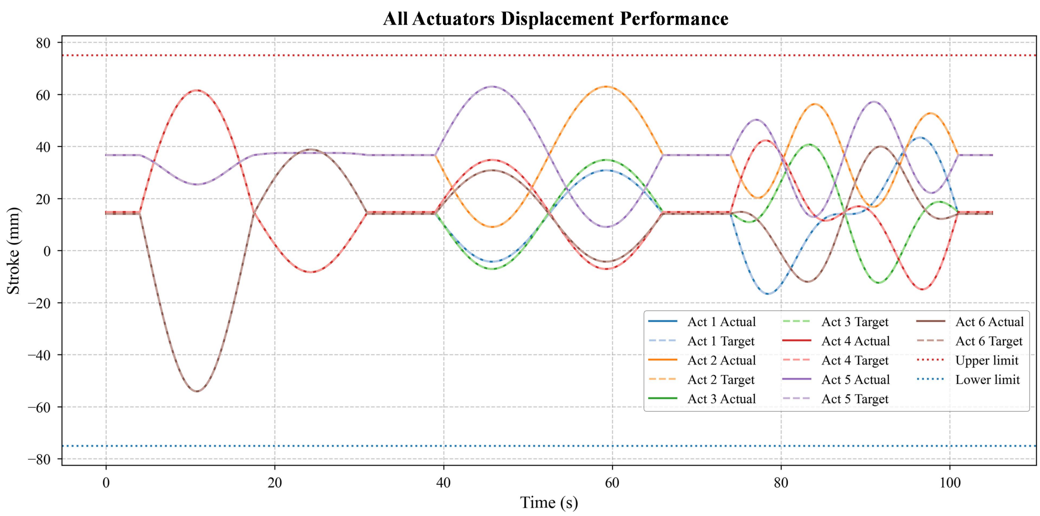

Figure 5. Actuator displacement commands and mechanical limits.

https://doi.org/10.3390/act15090485

As shown in Figure 5, all actuator displacement commands remain within the prescribed limits, indicating that the generated actuator-space commands are feasible for the selected rehabilitation trajectories.

5.3. Pose Accuracy Comparison

To intuitively illustrate the deviation caused by geometric mismatch, Figure 6 compares the simulated task-space tracking trajectories under the actual platform gaps of $h_1 = 54$ mm and $h_2 = 73$ mm. The curves depict the prescribed target trajectory, the simulated pose using the geometry-adaptive model, and the simulated pose utilizing the fixed-geometry assumption.

The simulated position and orientation errors for all five simulation cases are evaluated according to the unified task-space metrics defined in Section 4.5. For this evaluation, the measured spatial variables are substituted with the simulated platform position $\mathbf{p}_{\mathrm{sim}}(k)$ and rotation matrix $\mathbf{R}_{\mathrm{sim}}(k)$. Consequently, the quantitative pose accuracy results are summarized in Table 1.

The results in Table 1 reveal that the tracking errors remain relatively small only when the kinematic model assumption precisely matches the actual worn geometry. For instance, the adaptive model consistently yields minimal errors across all actual gap conditions. Furthermore, the fixed-geometry model performs accurately only when the actual gaps incidentally match its assumed 20 mm and 30 mm parameters. However, when this fixed assumption is applied to unmatched actual gaps, significant model-induced position and orientation errors emerge. Therefore, these theoretical deviations establish the importance of geometry-adaptive anchor-point reconstruction prior to hardware validation.

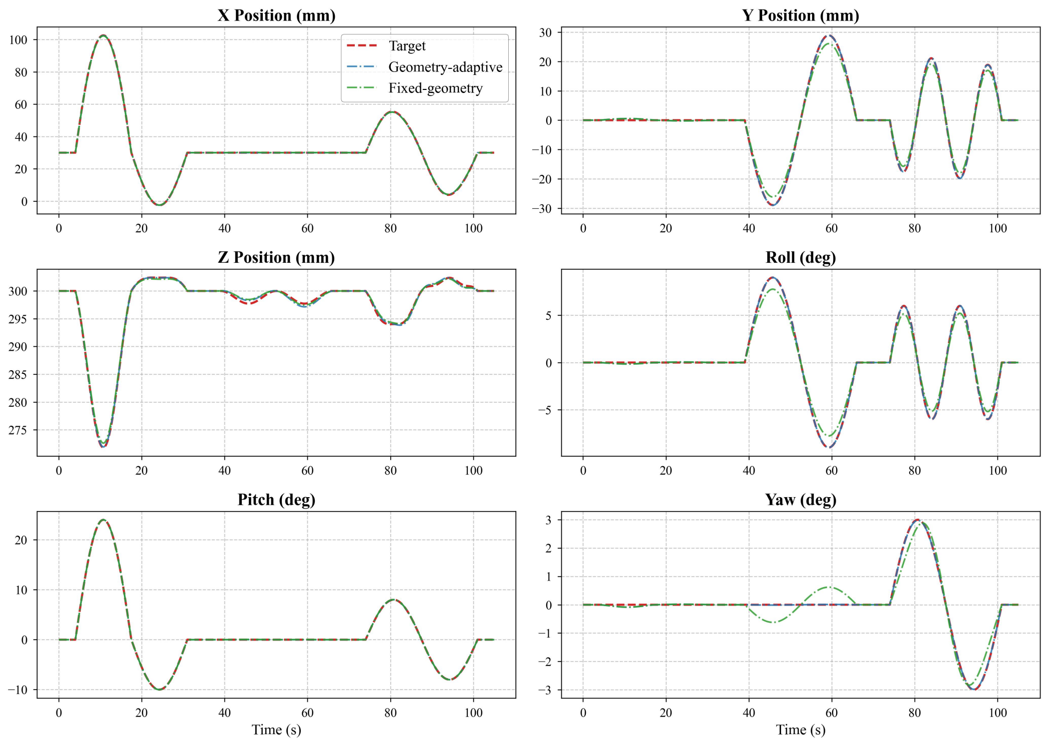

Figure 6. Comparison of simulated pose tracking with fixed and adaptive geometry.

Table 1. Overall simulated pose errors under different geometric assumptions and actual platform gaps.

Actual Gaps h_1, h_2 (mm)	Kinematic Model Assumption	Pos. RMSE (mm)	Max. Pos. Error (mm)	Ori. RMSE (deg)	Max. Ori. Error (deg)
0, 0	Fixed (20, 30)	2.15	4.76	0.53	1.20
0, 0	Adaptive (0, 0)	1.68	3.67	0.06	0.22
20, 30	Fixed or Adaptive	0.97	2.10	0.06	0.20
54, 73	Fixed (20, 30)	1.30	2.86	0.62	1.38
54, 73	Adaptive (54, 73)	0.32	0.58	0.05	0.18

6. Prototype Experiments

To comprehensively validate the proposed geometry-adaptive mechanism and kinematic model, prototype experiments are conducted to evaluate actuator-space tracking performance and task-space motion consistency. The experimental evaluation is divided into a human-worn proof-of-concept study and a rigid testbench comparative study.

6.1. Experimental System Setup

For all subsequent experiments, the control and measurement hardware setup remains consistent. The experimental system consists of the exoskeleton prototype, six integrated linear actuators, a host computer, an FDCAN communication module, and an optical motion-capture system (ChingMu). The prototype and experimental setup are shown in Figure 7. The total mass of the wearable prototype is 2813 g, with the upper platform, lower platform, and six linear actuation units weighing 575 g, 816 g, and 1422 g (237 g each), respectively.

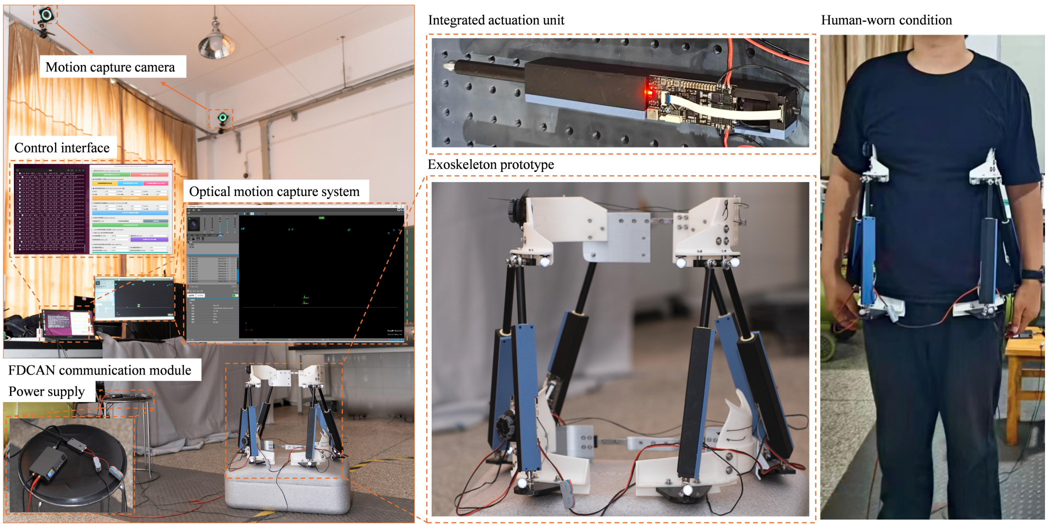

Figure 7. Prototype and experimental setup.

To ensure mechanical safety during the hardware operations, software-level current saturation limits (0.3 A per motor on the embedded driver boards, corresponding to a theoretical maximum axial force limit of $F_{\text{lim}}^{\text{theory}} = \frac{2\pi\eta K_t}{p_s} I_{\text{lim}} \approx 101.8$ N, with a 1.5 A current ceiling on the master power supply), real-time velocity clamping, and a dedicated hardware emergency-stop switch are applied in addition to the mechanical hard end-stops of the actuators, which constrain the linear displacement within ± 75 mm, and trajectory low-pass filtering to suppress mechanical jerks.

To accurately measure the task-space motion without being affected by global base movements, rigid marker clusters are attached to both the upper and lower platforms. The motion-capture system records their homogeneous transformation matrices in the world frame $\{W\}$ in real time, denoted as ${}^{W}\mathbf{T}_P(t)$ and ${}^{W}\mathbf{T}_B(t)$, respectively. The relative pose of the upper platform with respect to the lower base is calculated as

$$
{}^{B}\mathbf{T}_P(t) = \left({}^{W}\mathbf{T}_B(t)\right)^{-1}{}^{W}\mathbf{T}_P(t), \tag{37}
$$

from which the experimental position vector $\mathbf{p}(t)$ and Euler angles $\alpha(t), \beta(t), \gamma(t)$ are extracted. Data synchronization between the Robot Operating System (ROS) environment on the host computer and the motion-capture system is achieved using aligned absolute world time timestamps.

6.2. Human-Worn Validation

The general control and sampling parameters are summarized in Table 2, where FE, LB, and FC denote flexion/extension, lateral bending, and figure-eight circumduction trajectories, respectively. To validate the motion-generation capability and body-size adaptability of the proposed system, human-worn experiments were conducted with three healthy adult male volunteers having distinct anthropometric dimensions (Table 3). After the upper and lower split semi-ring platforms were worn and locked, the user-specific transverse gaps (h_1 and h_2) were measured to reconstruct the anchor-point coordinates.

Table 2. Experimental control and trajectory amplitude parameters.

Control Parameter	Value	Trajectory Parameter	Value
Upper-level loop	1 kHz	Flexion/extension (A_f/A_e)	$+24.0°/-10.0°$
Current loop	20 kHz	Lateral bending (A_l/A_r)	$+9.0°/-9.0°$
Position stiffness K_p	150 N/mm	Circumduction (A_f, A_l, A_a)	$8.0°, 6.0°, 3.0°$
Velocity damping K_d	$2\ \mathrm{N \cdot s/mm}$	Evaluated motions	FE, LB, FC

Table 3. Participant anthropometric characteristics and measured transverse gaps.

Participant	Height (cm)	Weight (kg)	Upper Gap h_1 (mm)	Lower Gap h_2 (mm)
Subject 1	172	63	64	40
Subject 2	178	73	70	47
Subject 3	176	84	104	64

The three rehabilitation trajectories were executed by each participant on the wearable prototype. The experimental tracking results are illustrated in Figure 8, organized into three columns for the FE, LB, and FC motions. The top row depicts human motion schematics and the corresponding X–Y plane trajectories. The second row displays the representative actuator displacement tracking curves for Subject 1, as all three subjects exhibited similarly precise actuator tracking. The subsequent six rows compare the task-space tracking responses of all three participants (Subjects 1–3) against the target trajectories across three positions (X, Y, Z) and three orientations (Roll, Pitch, Yaw).

For actuator-space analysis, the tracking error of the ith actuator is defined as $e_{q_i}(k) = q_{d,i}(k) - q_i(k)$, where $q_{d,i}(k)$ and $q_i(k)$ are the desired and measured displacements at the kth sampling instant, respectively. The overall displacement RMSE and maximum displacement error are calculated as

$$
\mathrm{RMSE}_q = \sqrt{\frac{1}{6N}\sum_{i=1}^{6}\sum_{k=1}^{N} e_{q_i}^2(k)}, \qquad e_q^{\max} = \max_{i,k}\left|e_{q_i}(k)\right|. \tag{38}
$$

Actuator-space and task-space tracking performance were evaluated using the unified metrics defined in Section 4.5. The quantitative experimental results across all participants are summarized in Table 4.

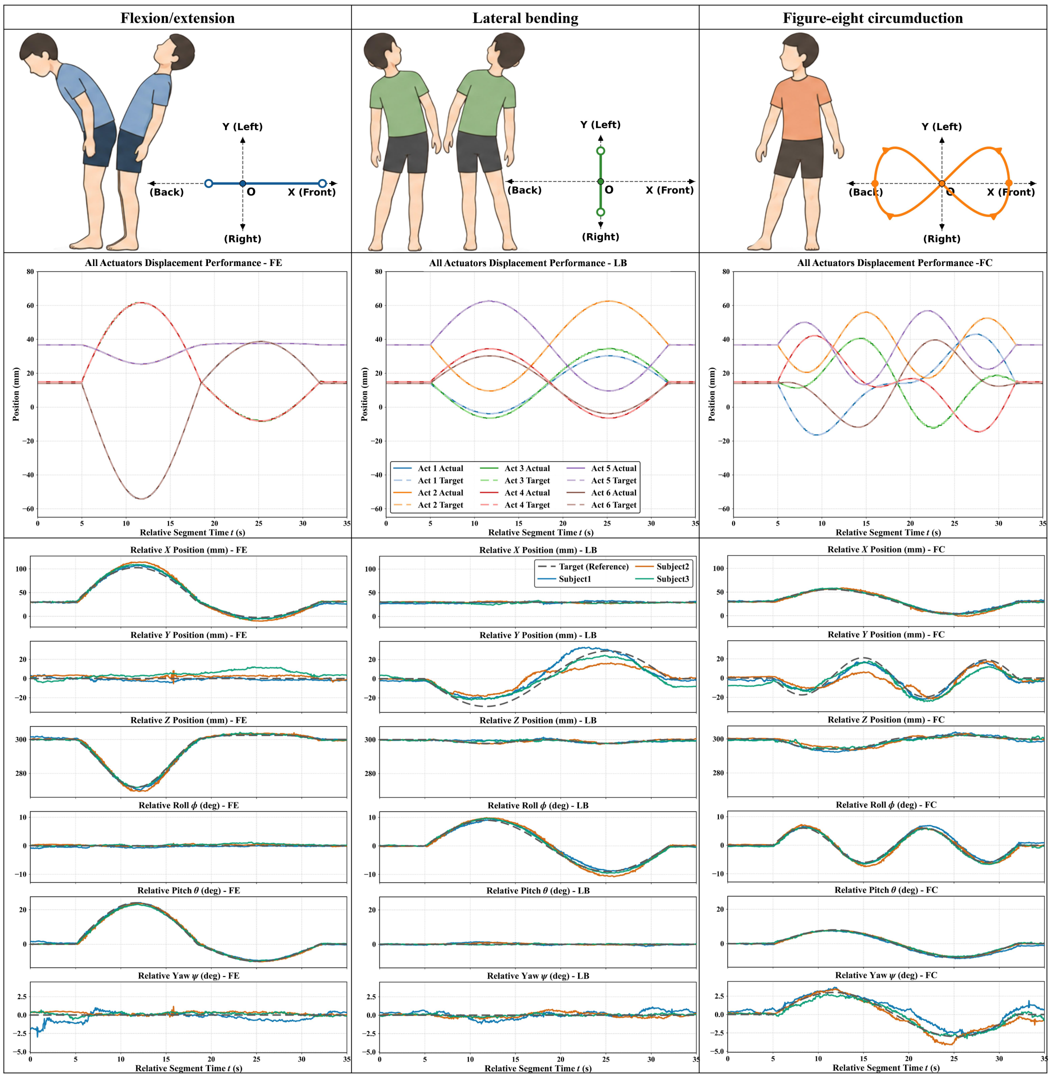

Figure 8. Experimental tracking results across participants.

Table 4. Experimental tracking errors across participants and rehabilitation motions.

Participant	Motion	Disp. RMSE (mm)	Disp. Max (mm)	Pos. RMSE (mm)	Pos. Max (mm)	Ori. RMSE (deg)
Subject 1	FE	0.10	0.79	3.79	9.44	1.07
	LB	0.09	0.48	6.17	12.26	0.99
	FC	0.09	0.75	4.21	8.97	1.22
	Global	0.09	0.79	4.73	12.26	1.09
Subject 2	FE	0.08	0.77	6.88	14.75	0.94
	LB	0.09	0.49	8.74	16.44	1.10
	FC	0.08	0.59	7.67	17.31	1.00
	Global	0.08	0.77	7.64	17.31	1.01
Subject 3	FE	0.09	0.70	6.92	13.01	0.84
	LB	0.09	0.53	5.66	10.18	0.58
	FC	0.08	0.58	5.73	10.43	0.71
	Global	0.08	0.70	6.01	13.01	0.71

Across all three participants, the linear actuators tracked the displacement commands accurately, yielding global displacement RMSEs between 0.08 mm and 0.09 mm with maximum displacement errors below 0.79 mm. At the task-space level, the global position RMSE ranged from 4.73 mm to 7.64 mm, and the global orientation RMSE remained between 0.71° and 1.09°. As observed from the trajectory tracking profiles in Figure 8, task-space deviations were primarily concentrated along the transverse (Y) axis, attributable to the structural flexibility of the sheet-like 3D-printed brackets and strapping interface compliance. It should be noted that this accuracy refers to the motion of the exoskeleton platform measured by marker clusters, not to the directly measured motion of the lumbar spine. Owing to the split semi-ring platform design, nominal anchor coordinates remain fixed within the rigid modules, constraining wearing-induced geometric variations exclusively to the 1D transverse increments h_1 and h_2. The prominent yaw deviation observed under geometric mismatch is consistent with the analytical sensitivity derived in Equations (18)–(20), where contralateral differential branch variations couple directly with the vertical rotational axis through the inverse Jacobian mapping.

These multi-subject results demonstrate the preliminary motion-generation feasibility of the geometry-adaptive parallel exoskeleton system across the tested range of body dimensions.

6.3. Rigid Testbench Validation

To remove these uncontrollable human-device compliance and interface motions and test the kinematic accuracy under rigid mounting, a comparative test was conducted on a rigid testbench without human involvement.

The prototype was fixed with actual transverse gaps of $h_1 = 54$ mm and $h_2 = 73$ mm. Two sets of actuator commands were generated and executed for comparison: one using a baseline fixed-geometry model (which assigned nominal default values of $h_1 = 20$ mm and $h_2 = 30$ mm) and the other using the proposed geometry-adaptive model with the actual measured gaps.

The quantitative task-space pose errors under the two modeling conditions are summarized in Table 5, and the corresponding pose tracking trajectories are compared in Figure 9. The results demonstrate that generating commands based on an inaccurate fixed-geometry assumption leads to significant task-space deviations on the physical hardware. In contrast, the geometry-adaptive model correctly reconstructs the anchor points, thereby minimizing model-induced tracking errors on the physical prototype.

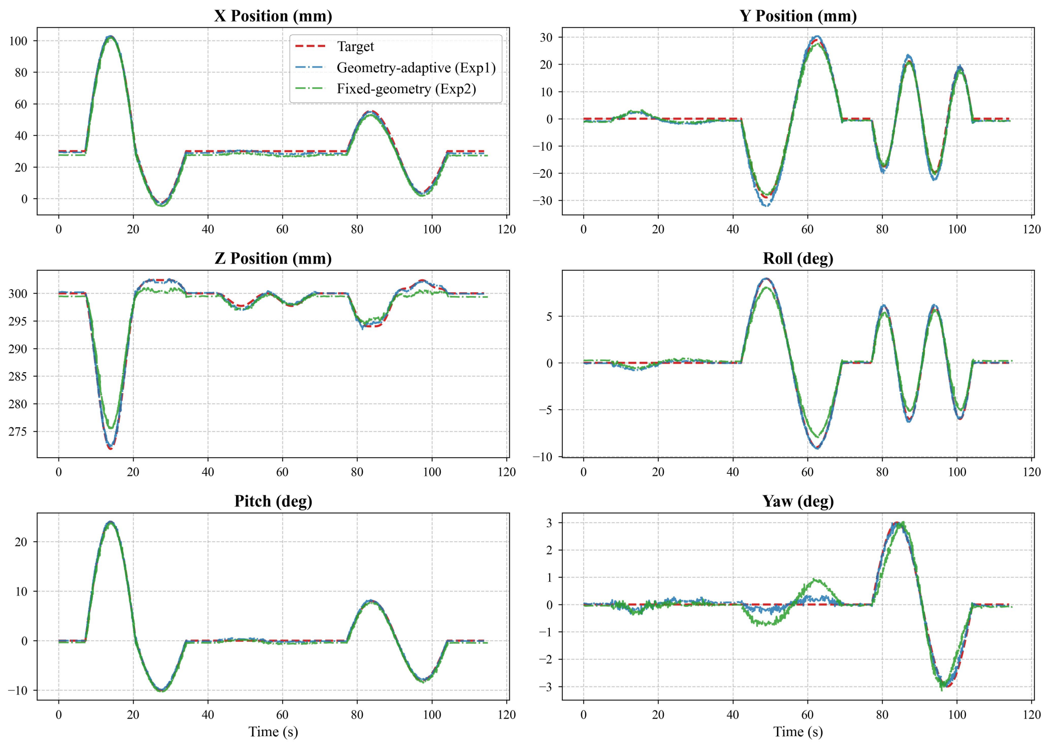

Figure 9. Task-space tracking results in the rigid testbench experiment.

Table 5. Overall pose errors in the rigid testbench experiment.

Model	Pos. RMSE (mm)	Max. Pos. Error (mm)	Ori. RMSE (deg)	Max. Ori. Error (deg)
Geometry-adaptive	1.86	4.14	0.34	1.02
Fixed-geometry assumption	3.07	8.02	0.78	2.04

7. Discussion

The geometry-adaptive kinematic model accounts for geometric inconsistencies in parallel lumbar exoskeletons. Simulations confirmed that anchor-point reconstruction based on transverse gaps (h_1 and h_2) reduces model-induced task-space deviations observed under fixed-geometry assumptions. This mathematical approach was validated on a rigid testbench, where the elimination of human compliance and structural flexibility confirmed the reduction of kinematic mapping errors. The kinematic model assumes locally rigid anchor points; soft-tissue deformation and interface sliding modify the effective anchor positions and transmitted forces and are not captured by the gap parameters, so the reported accuracy refers to the platform-level model rather than to the absolute motion of the human skeleton.

In human-worn experiments, the integrated linear actuators tracked the displacement commands with a global RMSE between 0.08 mm and 0.09 mm. However, the task-space tracking exhibited global position RMSEs ranging from 4.73 mm to 7.64 mm. As decomposed from the trajectory plots, this spatial error is primarily concentrated along the Y-axis, which is mainly attributed to the structural stiffness of the sheet-like 3D-printed prototype components and interface deformation. The progressive increase in position RMSE from simulation (0.32 mm) to the rigid testbench (1.86 mm) and human-worn testing (4.73–7.64 mm) reflects additional error sources progressively exposed across the experimental stages. The discrepancy between simulation and the rigid testbench is primarily attributed to physical manufacturing tolerances, joint clearances, and sensor measurement noise. When transitioning to human-worn operation, the error increase is predominantly driven by non-rigid human–device interaction effects rather than kinematic formulation failure. These effects primarily encompass biological soft-tissue compliance, strapping interface micro-sliding, human trunk impedance arising from incomplete motion compliance, and elastic deflection of the 3D-printed Y-axis supports. From a functional rehabilitation perspective, angular trajectory guidance is the primary clinical objective; the achieved orientation RMSE of approximately 1° represents a relative error of less than 8% against the target 18°–34° total range of motion, indicating that the major features of the commanded rotational trajectories were preserved during the present proof-of-concept experiments. A clinically acceptable tracking-error threshold for lumbar rehabilitation has not yet been established in this study and requires further clinical validation. Nevertheless, the sub-centimeter global position RMSE suggests promising spatial motion guidance under human-worn conditions in this preliminary evaluation. Beyond kinematic tracking accuracy, relevant criteria for evaluating lumbar rehabilitation include trunk muscle activation via surface electromyography (sEMG), interaction force distribution, and active range of motion; among these, electromyography analysis is planned as immediate future work upon integrating sEMG acquisition hardware.

Future work will focus on several aspects. First, because the current experiments evaluated kinematic trajectory tracking without archiving multichannel motor-current histories or implementing active force control, a coupled human–exoskeleton dynamic model alongside compliant force/impedance control will be formulated to regulate active interaction. Second, the 3D-printed structural components will be replaced with higher-stiffness materials to eliminate transverse bending, alongside ergonomic optimization of the binding interface. Finally, because individual actuator forces do not directly reflect human-perceived interaction forces due to strapping padding compliance, soft-tissue dissipation, and closed-chain parallel load distribution, extensive experiments incorporating synchronized motor-current logging, surface electromyography (sEMG) analysis, and interface pressure mapping will be carried out to directly evaluate physiological muscular unloading effects before clinical validation.

8. Conclusions

This paper presented a linear-actuator-driven parallel lumbar rehabilitation exoskeleton featuring a split semi-ring architecture to provide transverse width adjustability. To resolve the resulting geometric inconsistency between the physical worn state and the inverse kinematic model, a geometry-adaptive trajectory generation framework was developed utilizing measurable transverse gaps.

The proposed method was validated through simulation and proof-of-concept experiments. Multibody simulations demonstrated that compared with a fixed-geometry assumption, the geometry-adaptive approach reduced the theoretical position RMSE from 1.30 mm to 0.32 mm and the orientation RMSE from 0.62° to 0.05°. During human-worn experiments executing representative lumbar rehabilitation motions, the system achieved global actuator displacement RMSEs of 0.08–0.09 mm, task-space position RMSEs of 4.73–7.64 mm, and orientation RMSEs of 0.71°–1.09° across the three participants. Subsequently, rigid testbench comparative studies evaluated the mechanism under isolated rigid mounting conditions, confirming that the geometry-adaptive model effectively minimizes hardware-level positional deviations, reducing the testbench position RMSE from 3.07 mm to 1.86 mm and the orientation RMSE from 0.78° to 0.34° compared to the fixed-geometry model.

Overall, the proposed split semi-ring architecture and geometry-adaptive kinematic model provide preliminary proof-of-concept evidence for reducing configuration-induced kinematic inconsistencies in a variable-width parallel lumbar exoskeleton over the tested fitted-gap range. Further investigations involving improved structural stiffness, comprehensive dynamic interaction modeling, surface electromyography (sEMG) evaluation, and validation on larger patient cohorts will be conducted before clinical effectiveness is evaluated.

Author Contributions: Conceptualization, H.X. and G.G.; methodology, H.X. and P.C.; software, H.X.; validation, H.X. and Q.L.; formal analysis, H.X.; investigation, H.X., P.C. and Q.L.; data curation, H.X.; writing—original draft preparation, H.X.; writing—review and editing, G.G.; visualization, H.X.; supervision, G.G.; project administration, F.C. and G.G.; funding acquisition, F.C. and G.G. All authors have read and agreed to the published version of the manuscript.

Funding: This research was funded by the Yunnan Major Scientific and Technological Projects under Grant 202402AG050001.

Institutional Review Board Statement: The study was conducted in accordance with the Declaration of Helsinki, and approved by the Medical Ethics Committee of Kunming University of Science and Technology (Approval No. KMUST-MEC-213).

Informed Consent Statement: Informed consent was obtained from all subjects involved in the study. Written informed consent has been obtained from the participants to publish this paper and any accompanying identifiable images.

Data Availability Statement: The original contributions presented in the study are included in the article; further inquiries can be directed to the corresponding author.

Conflicts of Interest: The authors declare no conflicts of interest.

Abbreviations

The following abbreviations are used in this manuscript:

BLDC	Brushless direct current
DOF	Degree of freedom
sEMG	Surface electromyography
FDCAN	Flexible data-rate controller area network
FOC	Field-oriented control
PD	Proportional–derivative
RMSE	Root-mean-square error
ROS	Robot Operating System
UPS	Universal-prismatic-spherical
USDE	Unknown system dynamics estimator

References

1. Li, Y.; Zou, C.; Guo, W.; Han, F.; Fan, T.; Zang, L.; Huang, G. Global burden of low back pain and its attributable risk factors from 1990 to 2021: A comprehensive analysis from the Global Burden of Disease Study 2021. *Front. Public Health* **2024**, *12*, 1480779. [CrossRef]
2. Hayden, J.A.; Ellis, J.; Ogilvie, R.; Malmivaara, A.; van Tulder, M.W. Exercise therapy for chronic low back pain. *Cochrane Database Syst. Rev.* **2021**, *9*, CD009790. [CrossRef]
3. Zhou, T.; Salman, D.; McGregor, A.H. Recent clinical practice guidelines for the management of low back pain: A global comparison. *BMC Musculoskelet. Disord.* **2024**, *25*, 344. [CrossRef]
4. Park, C.H.; Beom, J.; Chung, C.K.; Kim, C.H.; Lee, M.Y.; Park, M.W.; Kim, K.; Chung, S.G. Long-term effects of lumbar flexion versus extension exercises for chronic axial low back pain: A randomized controlled trial. *Sci. Rep.* **2024**, *14*, 2714. [CrossRef]
5. Baltrusch, S.J.; van Dieën, J.H.; Koopman, A.S.; Näf, M.B.; Rodriguez-Guerrero, C.; Babič, J.; Houdijk, H. SPEXOR passive spinal exoskeleton decreases metabolic cost during symmetric repetitive lifting. *Eur. J. Appl. Physiol.* **2020**, *120*, 401–412. [CrossRef]
6. Zou, H.; Choi, J.; Kang, S.H.; Kim, S.; Jin, S. Passive exoskeletons alter low back load transfer mechanism. *J. Biomech.* **2023**, *147*, 111437. [CrossRef]
7. Madinei, S.; Nussbaum, M.A. Estimating lumbar spine loading when using back-support exoskeletons in lifting tasks. *J. Biomech.* **2023**, *147*, 111439. [CrossRef]
8. Johns, J.; Schultes, I.; Heinrich, K.; Potthast, W.; Glitsch, U. Biomechanical analysis of different back-supporting exoskeletons regarding musculoskeletal loading during lifting and holding. *J. Biomech.* **2024**, *168*, 112125. [CrossRef]
9. Ji, X.; Wang, D.; Li, P.; Zheng, L.; Sun, J.; Wu, X. SIAT-WEXv2: A wearable exoskeleton for reducing lumbar load during lifting tasks. *Complexity* **2020**, 8849427. [CrossRef]
10. Moulart, M.; Olivier, N.; Giovanelli, Y.; Marin, F. Subjective assessment of a lumbar exoskeleton's impact on lower back pain in a real work situation. *Heliyon* **2022**, *8*, e11420. [CrossRef]
11. Lüder, T.; Meier, M.; Neuweiler, R.; Lambercy, O. Evaluation of the support provided by a soft passive exoskeleton in individuals with back pain. *Appl. Ergon.* **2025**, *127*, 104514. [CrossRef]
12. Schrøder Jakobsen, L.; Samani, A.; Desbrosses, K.; de Zee, M.; Steinhilber, B.; Madeleine, P. Effects of 24-weeks in-field use of a back-supporting exoskeleton on biomechanics, work intensity and musculoskeletal discomfort: A randomized controlled trial among logistic workers. *Appl. Ergon.* **2025**, *125*, 104469. [CrossRef]
13. Ratke, E.J.; McMaster, H.; Vellucci, C.L.; Larson, D.J.; Holmes, M.W.R.; Beaudette, S.M. Ability of a passive back support exoskeleton to mitigate fatigue related adaptations in a complex repetitive lifting task. *J. Biomech.* **2025**, *181*, 112553. [CrossRef]
14. Qu, Y.; Wang, X.; Tang, X.; Liu, X.; Hao, Y.; Zhang, X.; Liu, H.; Cheng, X. A review of wearable back-support exoskeletons for preventing work-related musculoskeletal disorders. *Biomimetics* **2025**, *10*, 337. [CrossRef]
15. Dal Prete, A.; Gandolla, M.; Andreoni, G.; Braghin, F. Low back exoskeletons in Industry 5.0: From machines to perceiving co-pilots—A state-of-the-art review. *Sensors* **2025**, *25*, 1958. [CrossRef]
16. Mohamed Refai, M.I.; Moya-Esteban, A.; van Zijl, L.; van der Kooij, H.; Sartori, M. Benchmarking commercially available soft and rigid passive back exoskeletons for an industrial workplace. *Wearable Technol.* **2024**, *5*, e6. [CrossRef]
17. Park, J.-H.; Stegall, P.R.; Roye, D.P.; Agrawal, S.K. Robotic spine exoskeleton (RoSE): Characterizing the 3-D stiffness of the human torso in the treatment of spine deformity. *IEEE Trans. Neural Syst. Rehabil. Eng.* **2018**, *26*, 1026–1035. [CrossRef]
18. Farhadiyadkuri, F.; Popal, A.M.; Paiwand, S.S.; Zhang, X. Interaction dynamics modeling and adaptive impedance control of robotic exoskeleton for adolescent idiopathic scoliosis. *Comput. Biol. Med.* **2022**, *145*, 105495. [CrossRef]
19. Hou, C.; Wang, H.; Liu, F. A wearable exoskeletal lumbar spinal rehabilitation robot based on sliding mode control scheme. *Robot. Auton. Syst.* **2025**, *193*, 105063. [CrossRef]

20. Hou, C.; Yin, Z.; Wu, D.; Qian, R.; Tian, Y.; Wang, H. Design and kinematic and dynamic analysis simulation of a biomimetic parallel mechanism for lumbar rehabilitation exoskeleton. *Machines* **2025**, *13*, 728. [CrossRef]
21. Li, S.; Wang, H.; Li, M.; Tang, S.; Zhang, W. Kinematics and performance analysis of a parallel 4-UPS/RRR trunk rehabilitation robot. *J. Mech. Sci. Technol.* **2024**, *38*, 6319–6333. [CrossRef]
22. Huang, X.; Huang, L.; Shi, L.; Xu, L.; Cao, C.; Wu, H.; Cao, M.; Lv, C.; Shi, P.; Zhang, G.; Fang, F. Evaluation of the efficacy of a novel lumbar exoskeleton with multiple interventions for patients with lumbar disc herniation: A multicenter randomized controlled trial of non-inferiority. *Front. Bioeng. Biotechnol.* **2024**, *12*, 1520610. [CrossRef]
23. Rockenfeller, R.; Müller, A.; Damm, N.; Kosterhon, M.; Kantelhardt, S.R.; Frank, R.; Gruber, K. Muscle-driven and torque-driven centrodes during modeled flexion of individual lumbar spines are disparate. *Biomech. Model. Mechanobiol.* **2021**, *20*, 267–279. [CrossRef]
24. Na, J.; Jing, B.; Huang, Y.; Gao, G.; Zhang, C. Unknown system dynamics estimator for motion control of nonlinear robotic systems. *IEEE Trans. Ind. Electron.* **2020**, *67*, 3850–3859. [CrossRef]

https://doi.org/10.3390/act15090485